

Theoretical and Experimental Study of Supersonic Steady Flow around Inclined Bodies of Revolution

JOHN V. RAKICH* AND JOSEPH W. CLEARY†
NASA Ames Research Center, Moffett Field, Calif.

A three-dimensional method of characteristics is described and numerical results are critically assessed by comparison with the results of hypersonic wind-tunnel experiments. Calculations for a 15° half-angle sphere-cone have been performed for angles of attack up to $\alpha = 20^\circ$, and have been carried downstream 44 nose radii for $\alpha = 10^\circ$. Comparisons with pointed-cone calculations show that effects of bluntness persist at this distance. Pitot pressure distributions in the flowfield are in good agreement with experiment except on the leeward side of the body far from the nose, where low-energy, viscous fluid accumulates. The present calculations for 20° angle of attack indicate the formation of an embedded shock on the leeward side of the 15° sphere cone. Theoretical upwash angles around a Sears-Haack body are compared with classical slender body theory, indicating nonlinearities due to Mach number which may reduce the interference lift of wing-body combinations.

Nomenclature

a	= speed of sound
C_1, C_2, C_3	= bicharacteristic directions
C_1^*, C_2^*	= characteristic directions in meridional planes
C_p	= pressure coefficient
$C_{p,p}$	= Pitot pressure coefficient
h	= enthalpy
H	= total enthalpy
\bar{K}	= coefficient of numerical diffusion term [Eq. (18)]
k	= smooth constant [Eq. (18)]
l_m	= length of nose from tip to point of maximum thickness
M	= Mach number
n	= streamline normal lying in a meridional plane
p	= pressure
r	= radial distance from body axis
r_b	= body base radius, 0.5 ft for air and 0.094 ft for helium tests
Re	= Reynolds number, $V_\infty r_b / \nu_\infty$
R_n	= body nose radius
s	= streamline direction
s^*	= projection of s on meridional plane
T	= temperature
u, v, w	= velocity components along x , r , and ϕ
V	= total velocity ($V = \sqrt{Vs}$)
x	= axial distance from blunt nose
y	= lateral distance from model centerline
x, r, ϕ	= cylindrical coordinates
s, n, t	= streamline coordinates
ξ, η, ζ	= nonorthogonal shock-layer coordinates
α	= angle of attack
β	= $(M^2 - 1)^{1/2}$
γ	= specific heat ratio
δ	= shock angle in cross plane [Eq. (13)]
ϵ	= upwash angle, $\epsilon = -\varphi$
η	= body surface normal
θ	= flow angle from x axis in meridional plane, $\tan^{-1}v/u$
θ_c	= cone half angle
μ	= Mach angle, $\sin^{-1}(1/M)$
μ^*	= projection of μ on meridional plane
ν	= kinematic viscosity coefficient
ρ	= density
σ	= shock angle in meridional plane [Eq. (12)]
φ	= crossflow angle, $\sin^{-1}(w/V)$
Φ	= azimuthal angle, cylindrical coordinates

Subscripts

A, B	= initial and new data lines
b	= body
e	= edge of boundary layer
j, τ	= indices for radial position of mesh points (Fig. 2); $j = 1, \dots, J$
n	= body nose
N	= component normal to windward ray of cone
S	= shock
t	= total
u	= local upwash
w	= wall condition
∞	= freestream condition

Superscripts

i	= index for axial position of mesh point
$*$	= quantity or component referenced to meridional plane

Introduction

RECENT advances in computer technology have allowed complex three-dimensional flow calculations which were previously impractical. The theory of three-dimensional supersonic flow has been well developed for many years, so it is not surprising that several computational methods have been developed almost simultaneously in the last few years. The numerical techniques employed include variations based on the theory of characteristics¹⁻⁸ as well as on noncharacteristic methods.⁹⁻¹⁰ Chushkin¹¹ recently reviewed characteristics methods generally and described in detail four methods developed in the USSR. In presenting sample results illustrating proposed numerical techniques, analysts have often failed to make adequate comparisons with experiment. This paper is intended to fill this gap by making a more detailed comparison of recent numerical and experimental results.

Numerical methods for calculating three-dimensional flows by the method of characteristics may be divided into two general groups: 1) bicharacteristic methods¹⁻⁴ and 2) reference plane or semicharacteristic methods.⁵⁻⁸ The basic simplification obtained from characteristic theory involves the fact that the compatibility equations contain derivatives in one less direction than the number of space dimensions. Thus, in this sense, the three-dimensional characteristic equations are similar to those for two-dimensional noncharacteristic methods. Characteristic methods based on the use of reference planes simplify the finite-difference mesh and minimize

Presented as Paper 69-187 at the AIAA 7th Aerospace Sciences Meeting, New York, January 20-22, 1969; submitted February 17, 1969; revision received August 8, 1969.

* Research Scientist. Associate Fellow AIAA.

† Research Scientist. Member AIAA.

Finally, there are the usual energy and state equations

$$h + V^2/2 = H \quad (8)$$

and

$$h = h(p, \rho) \quad (9a)$$

$$a = a(p, \rho) \quad (9b)$$

The boundary conditions on the body may be formally written as

$$\theta = \theta_b(x; \Phi) \quad (10)$$

and on the shock as

$$u^v = G^v(\sigma; \delta, \Phi, \alpha) \quad (11)$$

Here $u^v = p, \theta, \phi, \rho$ for $v = 1, 2, 3, 4$. The shock angles σ and δ are defined by

$$\sigma = \tan^{-1}(\partial r_s / \partial x)_\Phi \quad (12)$$

and

$$\delta = \tan^{-1}(\partial \log r_s / \partial \Phi)_x \quad (13)$$

We now turn to a description of the numerical procedure used to solve Eqs. (4-9).

Finite Difference Equations

An arbitrary field point is identified by indices i, j, k in the manner shown in Fig. 2 for a typical reference plane Φ_k . We identify with superscripts $i-1$ and i the initial data line $\xi = \xi_A$ and the new data line $\xi = \xi_B$. Let the subscripts j and k denote the radial and circumferential positions of the mesh points. The subscript k will be omitted for brevity in writing the difference equations.

The Hartree or inverse method used requires interpolated data at the points of intersection on ξ_A of the characteristics through point i, j on ξ_B . A three-point Lagrange interpolation is used to determine the necessary data from known conditions at neighboring mesh points.

Three intersections are required for each field point on ξ_B . To identify these points, the convention is adopted in which the subscript τ represents the intersection with ξ_A of the streamline s^* through point i, j , and the subscripts $\tau-1$ and $\tau+1$ represent intersections of characteristics C_1^* and C_2^* , respectively (see Fig. 2).

With this convention, the compatibility equations (4) and (5) can be written in the following finite difference form:

$$A_1(p_i - p_{\tau-1}^{i-1}) + B_1(\theta_i - \theta_{\tau-1}^{i-1}) = F_1 \Delta C_1^* \quad (14)$$

$$A_2(p_i - p_{\tau+1}^{i-1}) + B_2(\theta_i - \theta_{\tau+1}^{i-1}) = F_2 \Delta C_2^* \quad (15)$$

Equations (6) and (7) for the streamline direction are approximated by

$$\varphi_j^i - \varphi_{\tau}^{i-1} = \left[F_3 + \bar{K} \frac{\varphi_{j-1}^{i-1} - 2\varphi_j^{i-1} + \varphi_{j+1}^{i-1}}{(\Delta\eta)^2} \right] \Delta s^* \quad (16)$$

$$\rho_j^i - \rho_{\tau}^{i-1} = \left[F_4 + \bar{K} \frac{\rho_{j-1}^{i-1} - 2\rho_j^{i-1} + \rho_{j+1}^{i-1}}{(\Delta\eta)^2} \right] \Delta s^* \quad (17)$$

Table 1 Test conditions

Test in	M_∞	Re_∞/ft	$T_i, ^\circ\text{R}$	P_i, psia
Air	10.6	1.2×10^6	2000	1200
Helium	14.9	9.2×10^6	545	1250

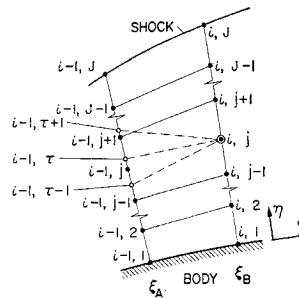


Fig. 2 Finite difference mesh.

where

$$\bar{K} = k(\Delta\eta)^2/2\eta_j\Delta\xi \quad (18)$$

The additional term on the right side of Eqs. (16) and (17) represents a diffusion process and is included to smooth oscillations that occur in certain extreme circumstances. It must be emphasized that the need for smoothing arises only when the computational mesh is coarse, relative to the flow-field gradients. This occurs in the entropy layer, for example. Experience indicates that the smoothing is not needed if the mesh is refined sufficiently, but that is not practical in three-dimensional problems where computation time and computer storage limitations are important factors. Therefore the proposed difference scheme provides a means for obtaining meaningful results with a relatively coarse mesh of points.

The arbitrary constant k in Eq. (18) is included to control the diffusion term. If $k = 0$ the diffusion is zero, and if $k = \eta_j/\Delta\eta$ the difference approximation becomes essentially what is known as the first-order Lax-Wendroff or Lax method.^{12,17} The Lax method provides too much diffusion,¹⁷ however, so k is chosen between 0 and $\eta_j/\Delta\eta$ in order to provide numerical stability without undue loss of accuracy. In present applications k has been set equal to one, and this condition is here termed a second-order Lax smoothing because $\bar{K} = 0$ ($\Delta\eta^2$). The adequacy of this finite difference approximation for present applications has been checked on axisymmetric flows.⁷

The finite-difference mesh used in most of the calculations presented here typically had 15 points between the body and shock on seven meridional planes. The required number of planes varies with angle of attack, and for small angles as few as three planes are sufficient. Pointed-cone solutions were obtained with nine meridional planes. Second-order smoothing was used for the pointed cone and only for x/R_n greater than about 10 for the blunted cone.

The step size $\Delta\xi = \xi_B - \xi_A$ (Fig. 1) was typically set equal to 80% of the maximum step allowed by the Courant-Friedrich-Lewy stability condition, that is, $\Delta\xi = 0.8 (\xi_m - \xi_A)$ where ξ_m is determined by the intersection with the body of the characteristic C_2^* through point $(i-1, 2)$. This condition was tested only on the windward side, which is usually the point that determines the maximum step size.

Results and Discussion

The method of characteristics described herein is generally applicable to smooth bodies with noncircular cross-sectional shapes, but present applications are restricted to pointed and blunt bodies of revolution. A large amount of experimental data has been collected for blunt cones which will allow critical evaluation of the present inviscid theory. Blunt-cone comparisons are divided into two sections, depending on whether the relative angle of attack α/θ_c is greater than or less than unity.

Experiments were performed in the Ames 3.5-ft Hypersonic Wind Tunnel in air, and in the Ames 20-in. tunnel in helium.¹³⁻¹⁴ Test conditions are given in Table 1. Tests in air were performed at $M_\infty = 10.6$ whereas the blunt-cone theory is for $M_\infty = 10$. This small difference should not affect the conclusions of this paper.

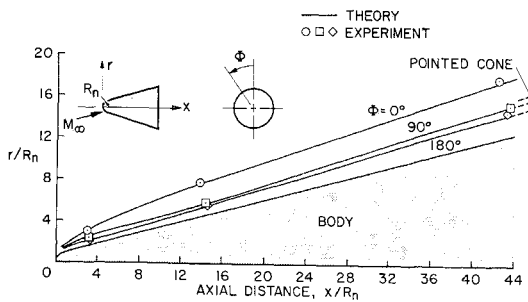


Fig. 3 Shock shape ($\theta_c = 15^\circ$, $\alpha = 10^\circ$, $M_\infty \approx 10$, $\gamma = 1.4$, $Re = 0.6 \times 10^6$).

15° Cone at 10° Angle of Attack

At hypersonic speeds, the bow shock around a blunt body can influence the flowfield far from the nose. It is therefore appropriate to begin with a look at the shock position, to shed light on flowfield properties shown later. Figure 3 shows the shock shape on three meridional planes $\Phi = 0^\circ$, 90° , and 180° . Agreement with experimental data available from Pitot surveys is good. Also shown (at the right margin of the figure) are limiting shock positions obtained from the pointed-cone solution. It is seen that the blunt-cone shock quickly reaches its limiting value for $\Phi = 90^\circ$ and 180° , but on the leeward side, $\Phi = 0^\circ$, it is still far from the pointed-cone shock, even at $x/R_n = 44$. The shock angle σ (measured in meridional planes) is shown in Fig. 4. Shock waves around blunted cones at zero angle of attack typically have a local minimum in the shock angle which causes the total pressure peak in the entropy layer. This minimum shock angle occurs at $x/R_n = 10$ for $\alpha = 0$. At 10° angle of attack the minimum point is shifted considerably, as seen in Fig. 4. On the leeward side of the cone a minimum angle of $\sigma_m = 18.38^\circ$ occurs at $x/R_n = 40.7$. Shock angles for the pointed cone are also shown in the figure.

Surface pressure distributions are shown in Fig. 5 for tests in air at $M_\infty \approx 10$ and in helium at $M_\infty = 14.9$. The distributions are similar in the two gases and agreement between theory and experiment is good. Except for the windward meridian in helium, the experimental pressures tend to be slightly higher than those predicted by theory, as might be expected from boundary-layer displacement effects. The shape of the pressure curves, with a minimum and a subsequent recompression to the conical value, closely follows the variation of shock angle shown in Fig. 4. The variation in pressure beyond $x/R_n = 12$ is very small as indicated by the pointed-cone results in Fig. 5a.

Pitot pressure distributions on body-normal lines are shown in Fig. 6 for three values of bluntness; distributions in three planes are presented for each station. The effect of the local minimum in the shock angle is evident in Fig. 6a for $\Phi = 180^\circ$, where a peak in pressure occurs just off the body. The numerical calculation rounds off the peak slightly but agree-

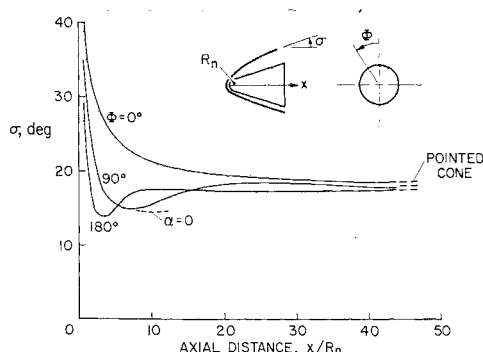


Fig. 4 Shock angle ($\theta_c = 15^\circ$, $\alpha = 10^\circ$, $M_\infty \approx 10$, $\gamma = 1.4$).

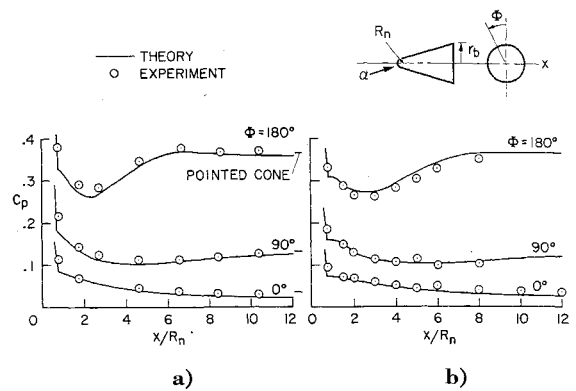


Fig. 5 Surface pressure ($\theta_c = 15^\circ$, $\alpha = 10^\circ$): a) Air ($\gamma = 1.4$, $M_\infty \approx 10$, $Re = 0.6 \times 10^6$); b) Helium ($\gamma = 1.667$, $M_\infty = 14.9$, $Re = 0.86 \times 10^6$).

ment with experiment is good otherwise. A theoretical maximum Pitot pressure can be calculated from the minimum shock angle (Fig. 4) and the calculated static pressure on the body at that station. This value is shown in Fig. 6 and is larger than both numerical and experimental values. Aside

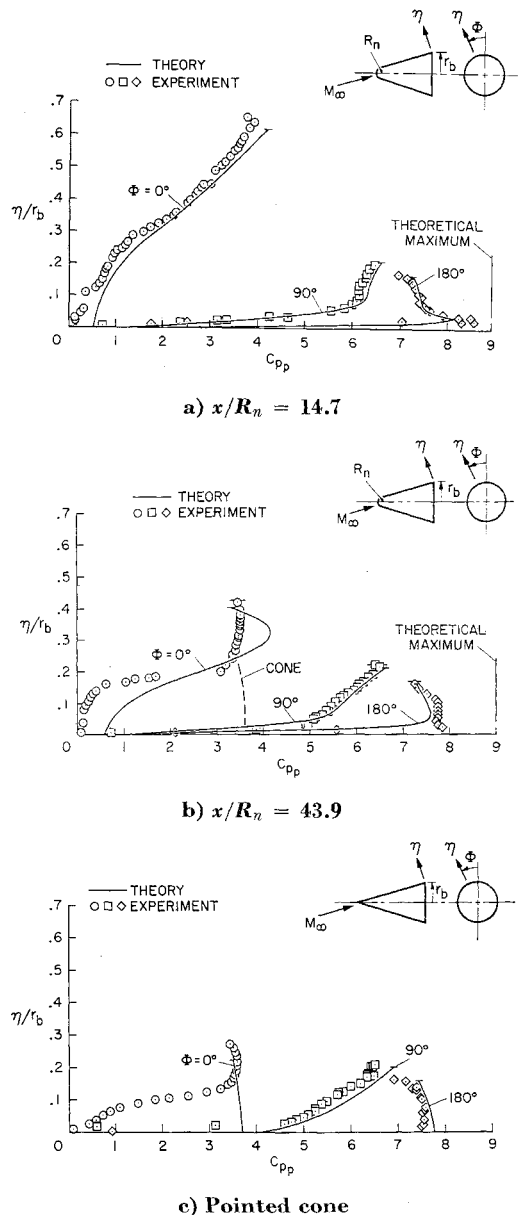


Fig. 6 Pitot pressure ($\theta_c = 15^\circ$, $\alpha = 10^\circ$, $M_\infty \approx 10$, $\gamma = 1.4$, $Re = 0.6 \times 10^6$).

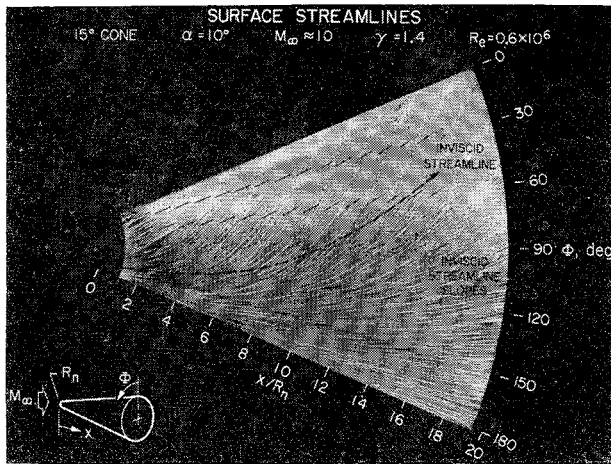


Fig. 7 Surface streamlines ($\theta_c = 15^\circ$, $\alpha = 10^\circ$, $M_\infty \approx 10$, $\gamma = 1.4$, $Re = 0.6 \times 10^6$).

from this point and the usual thin boundary layer, there do not appear to be any large-scale viscous effects for $x/R_n = 14.7$. The difference between theory and experiment on the leeward side, $\Phi = 0$, and for η/r_b less than 0.1, is attributed to a thickening of the boundary layer there.

Figure 6b shows the Pitot pressures for $x/R_n = 43.9$. Here a thick viscous layer seems to form near the body on the leeward side, as indicated by the low experimental Pitot pressures there. Although it is difficult to pinpoint the edge of the boundary layer in a region with large inviscid total pressure gradients, the knee in the pressure data at $C_{pp} \approx 0.5$ suggests that the boundary layer extends to about $\eta/r_b = 0.16$. Differences between theory and experiment closer to the shock are not completely understood. The lower experimental pressures on the leeward side between the boundary layer and the shock could be caused either by a loss of total pressure along a streamline due to viscous dissipation, or by boundary-layer displacement effects on the shock. The latter reason is believed more plausible. Although the shock is not greatly displaced, small angular changes can have a large effect on Pitot pressure.

On the windward side of the body, the peak Pitot pressure is lost in the calculation, but the experimental results are well predicted over most of the shock layer. The experimental data also show a reduced peak pressure from the maximum value for $x/R_n = 43.9$ (Fig. 6b). This suggests that most of the entropy layer has been swallowed by the boundary layer.

Results for the pointed cone are shown in Fig. 6c. Agreement with experiment is good on the windward and 90° planes, but large differences are observed on the leeward side. The viscous layer that began to form on the blunt cone (see Fig. 6b) is more pronounced for the pointed cone and also causes a large displacement of the shock wave, as shown by the Pitot-pressure data in Fig. 6c. Such effects have been noted previously by Tracy¹⁸ and others. This viscous layer is formed by the strong crossflow in the boundary layer that continually feeds low-energy fluid into the leeward region, where it is trapped.

To illustrate, and to obtain quantitative estimates of the strong viscous crossflow, an oil-film experiment was performed which produced the streamline pattern shown in Fig. 7. A sheet of paper was wrapped around the conical part of a blunted cone, coated with pigmented oil, and inserted in the wind tunnel for about 2 sec. After the run, the sheet was removed and laid flat to produce the developed cone surface shown in the figure. Overlaid on the experimental streamline pattern are inviscid velocity directions and a typical inviscid streamline. It is seen that the viscous streamlines turn (in the direction of decreasing pressure) much more than does the inviscid streamline.

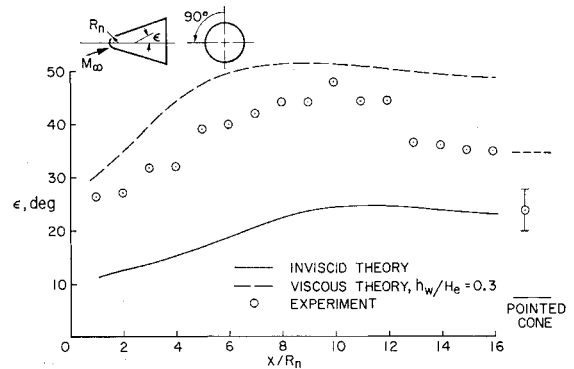


Fig. 8 Surface crossflow angles on 90° meridian ($\theta_c = 15^\circ$, $\alpha = 10^\circ$, $M_\infty \approx 10$, $\gamma = 1.4$, $Re = 0.6 \times 10^6$).

Faired stream angles measured from Fig. 7 are shown in Fig. 8 for the $\Phi = 90^\circ$ plane. Stream angles based on the small crossflow boundary-layer theory of Beckwith¹⁹ are also shown in Fig. 8. The viscous theory is for a wall enthalpy ratio of 0.3, which is the approximate experimental value. The axial variation of crossflow is predicted reasonably well, but the viscous theory is somewhat high. This is probably due to violations of assumptions made in the small crossflow theory. Pointed-cone results are shown on the right margin of Fig. 8. The viscous theory is from Moore's pointed-cone solution²⁰ for small angle of attack. An estimate of nonadiabatic wall effects for the pointed cone was made using Beckwith's theory.¹⁹

Just off the body surface the blunt-cone crossflow angles tend to the pointed-cone values in a nonuniform way, as shown in Fig. 9. The variation of crossflow angle normal to the body is shown for several axial positions. In the presence of bluntness the crossflow angles are largest near the body because of the lower momentum of the layer of fluid (entropy layer) which has passed through the steeper part of the bow-shock wave. This layer thins with distance from the nose and the pointed-cone crossflow angle is attained only at the outer edge of the layer. Close to the nose the boundary-layer edge conditions are those at the inner edge of the entropy layer. Far from the nose the boundary layer thickens and eats into the entropy layer so that the boundary-layer edge conditions tend to the pointed-cone values.

15° Cone at 20° Angle of Attack

For angles of attack greater than the cone half-angle, the flowfield changes in many important respects from the small-angle-of-attack flow. Indeed, except for the most windward part of the flow, the pointed-cone flow remains unsolved for the case where $\alpha > \theta_c$. However, many of the problems connected with the calculation of large-angle-of-attack flows are avoided near the nose of a blunt body; these results are discussed below.

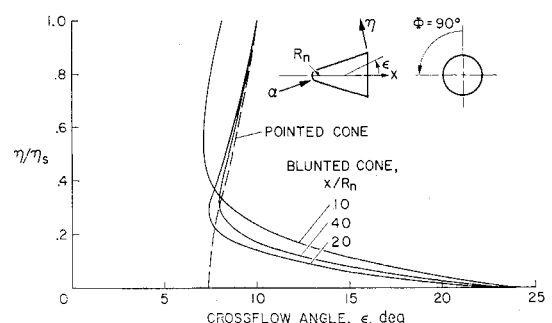


Fig. 9 Shock-layer crossflow angles in 90° plane ($\theta_c = 15^\circ$, $\alpha = 10^\circ$, $M_\infty \approx 10$, $\gamma = 1.4$).

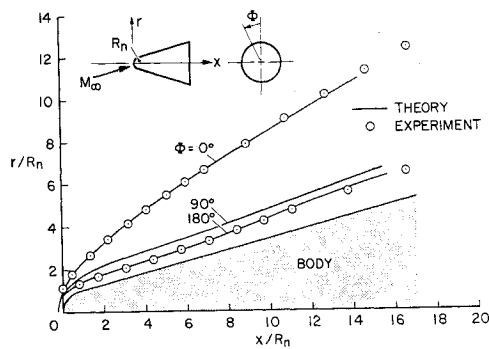


Fig. 10 Shock shape ($\theta_c = 15^\circ$, $\alpha = 20^\circ$, $M_\infty = 14.9$, $\gamma = 1.667$, $Re = 0.86 \times 10^6$).

Experiments with a blunt cone in helium have been performed for this case and are compared with theory in Figs. 10 and 11. Figure 10 shows the shock shape (experiment from a shadowgraph) and Fig. 11 shows the surface pressure distribution. Agreement with experiment again is good for the planes shown. The circumferential pressure distribution at $x/R_n = 8$ (Fig. 12) also shows good agreement between theory and experiment except on the $\Phi = 30^\circ$ plane, where the theoretical value tends to be low.

Inviscid calculations predict a pressure minimum near $\Phi = 30^\circ$ with a recompression of the flow approaching the leeward meridian. Physically unrealistic pressures are attained on the 30° meridian for x/R_n greater than 10 to 14, but the calculation can be extended farther downstream to obtain a valid solution on more windward meridians. Numerical difficulties arising from this low-pressure region⁶ prompted the study of an inviscid supersonic flow in the vicinity of a rear stagnation point. The usual argument is made that the flow far from the nose of a slender cone at large angle of attack is similar to that over a circular cylinder transverse to the freestream. In the absence of viscosity, the pressure distribution over a circular cylinder is that shown in Fig. 12.

The proposed inviscid flow near the rear stagnation point has a wake-like structure and is therefore termed an inviscid-wake model. As the supersonic flow expands around the cylinder, it will approach the rear stagnation point at the plane of symmetry where it must turn by 90° . Since this turning angle is too large for any oblique shock, the flow must undergo a normal shock before reaching the plane of symmetry. The shock position is not easily determined. However, if it is assumed that a stagnation point exists on the body at the rear plane of symmetry, and if it is also assumed that the pressure there is the freestream pressure, it is possible to determine the shock position. The assumption that $p = p_\infty$ at the rear stagnation point is consistent with Newtonian flow except that in the usual Newtonian wake the pressure is constant over the entire rear surface.

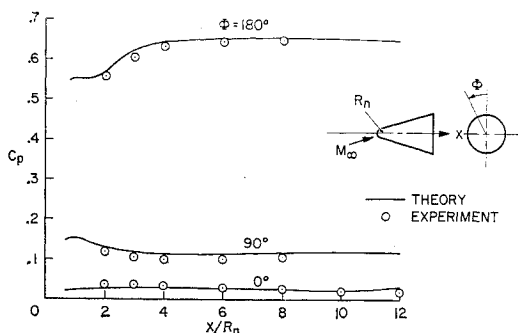


Fig. 11 Surface pressure ($\theta_c = 15^\circ$, $\alpha = 20^\circ$, $M_\infty = 14.9$, $\gamma = 1.667$, $Re = 0.86 \times 10^6$).

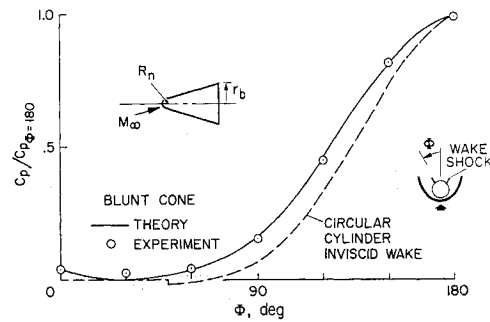


Fig. 12 Circumferential surface-pressure distribution at $x/R_n = 8$ ($\theta_c = 15^\circ$, $\alpha = 20^\circ$, $M_\infty = 14.9$, $\gamma = 1.667$, $Re = 0.86 \times 10^6$).

This argument suggests that a secondary shock must form some distance behind the nose of a blunt cone at large angles of attack. To study this possibility, surface Mach lines were calculated for the 15° cone at 20° angle of attack. A numerical integration was performed using local Mach line slopes from the described method of characteristics solution. The family of right running Mach lines obtained in this way are shown in Fig. 13. The most significant feature of this family of curves is their tendency to coalesce at about $x/R_n = 12$ and 15° off the leeward plane of symmetry. This clearly shows how the wake shock might form in an inviscid flow. Embedded shocks have been observed^{18,21} but it was not clear that they should occur in the absence of a viscous boundary layer.

The formation of embedded shocks on the leeward side of bodies at large angles of attack provides an explanation of difficulties encountered⁶ in extending inviscid flow solutions far downstream. These difficulties are now understood to arise from the physical features of the flow and not from the particular numerical technique employed. Any method of characteristics usually requires special treatment of shock waves in the flow. Work can proceed along these lines now that the problem is clarified. The calculation of flows over pointed cones at large angles of attack might also be reconsidered with allowance for secondary shocks.

Body-Induced Upwash

As a final application to demonstrate the flexibility of the present method, some features of the flow around a Sears-Haack body with fineness ratio of 6 are considered next. Such a body is typical of those considered for hypersonic aircraft. A question of continued interest is whether there is any possibility for interference lift on wing-body combinations at hypersonic speeds. One factor that affects the interference lift is the body-generated upwash, which can increase

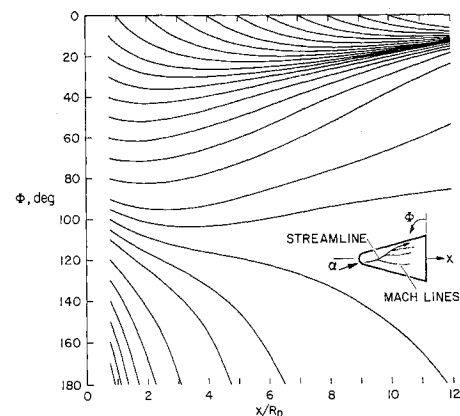


Fig. 13 Surface Mach lines ($\theta_c = 15^\circ$, $\alpha = 10^\circ$, $M_\infty = 10$, $\gamma = 1.4$).

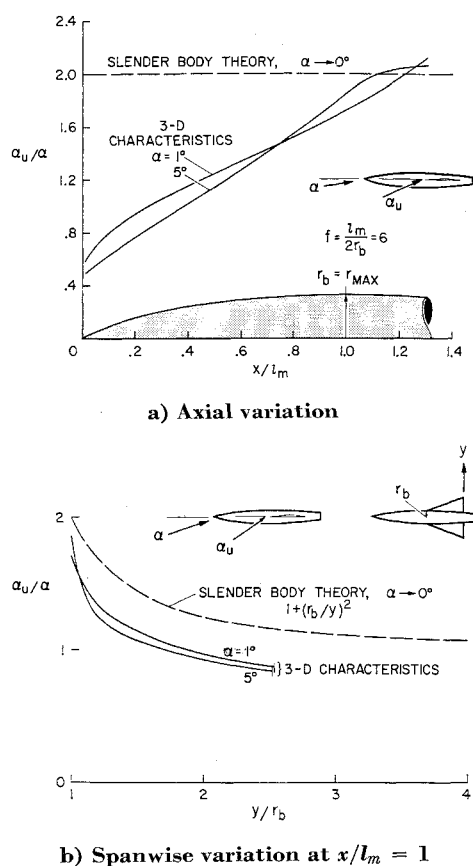


Fig. 14 Inviscid upwash on 90° plane (Sears-Haack body with fineness ratio 6, $M_\infty = 7.4$).

the local angle of attack of the wing.^{22,23} A wing immersed in the flowfield of the body sees a local angle of attack, which is given approximately by

$$\alpha_u/\alpha \approx -\varphi/\alpha \quad (19)$$

in the 90° plane and for slender bodies. Figure 14a shows the axial variation of this upwash angle normalized by the angle of attack of the body. At the apex the upwash has the pointed-cone value. (A pointed-cone tangent at 1% of body length was used for starting conditions in this calculation.) The upwash increases with distance from the nose, approaching the slender-body result of $\alpha_u/\alpha = 2$ near the point of maximum thickness. The relative upwash is not greatly changed up to 5° angle of attack.

Figure 14b shows the spanwise variation of upwash at the point of maximum thickness $x/l_m = 1$. The calculated variation is similar to the inverse-square decrease predicted by slender-body theory, but is displaced downward. The numerical result terminates at the bow shock and the relative upwash is less than 1 there; that is, the local angle of attack is positive but less than freestream inclination. This is due to a loss of the vertical component of momentum in crossing the shock.

Other calculations at lower Mach numbers have shown that slender-body theory gives an adequate prediction of upwash at $M_\infty = 2$ and not too close to the nose. The generally lower upwash angles presently shown for $M_\infty = 7.4$ suggest a decreased interference lift at hypersonic speeds.

Concluding Remarks

Detailed comparisons between theory and experiment have been made which illustrate some limitations of inviscid theory in predicting three-dimensional supersonic flows. The reliability of the present numerical methods is established by the

excellent agreement with experiment in areas free of large viscous effects. Present results indicate that the proposed method of characteristics can be applied as far downstream as desired, provided there are no embedded shocks in the flow. Nevertheless, a need for some improvements in the numerical method is suggested by the present study.

For small angles of attack, where the leeward meridian is positively inclined with respect to the freestream ($\alpha/\theta_c < 1$), accurate predictions of the complete flowfield will require an accounting of viscous interactions. The boundary layer on the leeward side of blunt bodies may only be considered thin relatively close to the nose. Therefore, in most cases thick aviscous layer and a strong viscous-inviscid interaction will develop.

Including a coupled boundary-layer calculation in the inviscid program may ease numerical problems in the inviscid entropy layer over blunt bodies, since the entropy layer will be swallowed by the boundary layer. However, an accurate calculation including the effect of external vorticity on the boundary layer may require a local refinement of the inviscid density calculation near the wall.

At large angles of attack ($\alpha/\theta_c > 1$) the flow on the leeward side of the body seems to be wakelike even in the inviscid limit. The recompression that occurs near the rear stagnation point suggests a secondary shock which must be allowed for in the inviscid calculation. The adverse pressure gradient that develops there makes the viscous-inviscid interaction problem a formidable one, but an essential one for understanding the separated flow behind inclined bodies.

References

- 1 Powers, S. A., Niemann, A. F., Jr., and Der, J., Jr., "A Numerical Procedure for Determining the Combined Viscid-Inviscid Flow Fields over Generalized Three-Dimensional Bodies," AFFDL-TR-67-124, Vol. 1, Dec. 1967, Air Force Systems Command.
- 2 Strom, C. R., "The Method of Characteristics for Three-Dimensional Real-Gas Flows Including the Digital Computer Program Details and Operating Procedures for Frozen Flows," AFFDL-TR-67-47, July 1967, Air Force Systems Command.
- 3 Sauerwein, H., "Numerical Calculation of Multidimensional and Unsteady Flows by the Methods of Characteristics," *Journal of Computational Physics*, Vol. 1, 1967, pp. 406-432.
- 4 Magomedov, K. M., "Method of Characteristics for Numerical Calculations of Three Dimensional Gas Flows," *Zhurnal Vychislitel'noy Matematiki i Matematicheskoy Fiziki*, Vol. 6, 1966, pp. 313-325.
- 5 Moretti, G. et al., "Flow Field Analysis of Reentry Configurations by a General Three-Dimensional Method of Characteristics," ASD-TR-67-727, Vol. III, Feb. 1962, Air Force Systems Command.
- 6 Rakich, J. V., "Three-Dimensional Flow Calculation by the Method of Characteristics," *AIAA Journal*, Vol. 5, No. 10, Oct. 1967, pp. 1906-1908.
- 7 Rakich, J. V., "A Method of Characteristics for Steady Three-Dimensional Supersonic Flow with Application to Inclined Bodies of Revolution," TN D-5341, 1969, NASA.
- 8 Katskova, O. N. and Chushkin, P. I., "Three-Dimensional Supersonic Equilibrium Flow of a Gas around Bodies at Angle of Attack," Translation TT F-9790, 1965, NASA.
- 9 Babenko, K. I. et al., "Three-Dimensional Flow of Ideal Gas past Smooth Bodies," Translation TT F-380, 1966, NASA.
- 10 Babenko, K. I. and Rusanov, V. V., "Difference Methods for Solving Three-Dimensional Problems in Gas Dynamics," Translation TT F-10,827, 1967, NASA.
- 11 Chuskin, P. I., "Three-Dimensional Supersonic Flows," *Progress in Aeronautical Sciences*, 1st ed., Vol. 9, edited by D. Küchemann, Pergamon Press, New York, 1968, pp. 41, 122.
- 12 Richtmeyer, R. D. and Morton, K. W., *Difference Methods for Initial Value Problems*, 2nd ed., Interscience, New York, 1967.
- 13 Cleary, J. W., "An Experimental and Theoretical Investigation of the Pressure Distribution and Flow Fields of Blunted Cones at Hypersonic Mach Numbers," TN D-2969, 1963, NASA.

¹⁴ Cleary, J. W., "Effects of Angle of Attack and Bluntness on the Shock Layer Properties of a 15° Cone at a Mach Number of 10.6," TN D-4909, 1968, NASA.

¹⁵ Rakich, J. V., "Numerical Calculation of Supersonic Flows of a Perfect Gas Over Bodies of Revolution at Small Angles of Yaw," TN D-2390, 1964, NASA.

¹⁶ Rakich, J. V., "Calculation of Hypersonic Flow over Bodies of Revolution at Small Angles of Attack," *AIAA Journal*, Vol. 3, No. 3, March 1965, pp. 458-464.

¹⁷ Richtmeyer, R. D., "A Survey of Difference Methods for Non-Steady Fluid Dynamics," TN 63-2, Aug. 1962, National Center for Atmospheric Research, Boulder, Colo.

¹⁸ Tracy, R., "Hypersonic Flow over a Yawed Circular Cone," Hypersonic Research Project Memo 69, Aug. 1963, California Institute of Technology.

¹⁹ Beckwith, I. E., "Similarity Solutions for Small Crossflows in Laminar Boundary Layers," TR R-107, 1961, NASA.

²⁰ Moore, F. K., "Laminar Boundary Layer on a Circular Cone in Supersonic Flow at a Small Angle of Attack," TN 2521, 1951, NACA.

²¹ Rainbird, W. J., "Turbulent Boundary-Layer Growth and Separation on a Yawed Cone," *AIAA Journal*, Vol. 6, No. 12, Dec. 1968, pp. 2410-2416.

²² Pitts, W. C., Nielsen, J. N., and Kaattari, G. E., "Lift and Center of Pressure of Wing-Body-Tail Combinations at Subsonic, Transonic and Supersonic Speeds," TR R-1307, 1957, NACA.

²³ Ferrari, C., "Wing-Body Interference at Supersonic Speeds," *Aerodynamic Components of Aircraft at High Speeds*, Chap. 5, Sec. C, edited by A. F. Donovan and H. R. Lawrence, Princeton Univ. Press, 1957.

MARCH 1970

AIAA JOURNAL

VOL. 8, NO. 3

Transition Experiments on a Flat Plate at Subsonic and Supersonic Speeds

F. K. OWEN*

University of Oxford, Oxford, England

A new method of detecting boundary-layer transition at supersonic speeds is described. The majority of methods such as schlieren and those of maximum surface temperature and peak surface Pitot pressure, locate positions near the end of transition, which, as will be shown in the paper, have a strong Mach number and unit Reynolds number dependence. A more complete picture of transition dependence on these parameters has been obtained by measuring the change in the root mean square of the voltage fluctuation across surface thin film gages operated at constant temperature. This technique enables the effects of Mach number and unit Reynolds number on the beginning and length of transition to be established more precisely than with previously used methods.

I. Introduction

SINCE transition from laminar to turbulent flow can account for significant changes in such important parameters as skin friction, heat transfer, and wake structure, it is important that the variation of transition Reynolds number with Mach number be accurately determined. However, there is much speculation at present regarding the effects of Mach number and unit Reynolds number on transition, although much of the scatter in the data can be attributed to differences in the methods used in observing transition and, as recently reported in Ref. 1, to differences in wind-tunnel disturbance levels. But the problem is complicated still further by the difficulty of isolating the large number of individual factors that are known to effect transition at supersonic speeds.

An insight into the mechanism of transition has resulted from records of velocity fluctuations in transition regions measured by hot wires showing intermittent bursts of laminar and then turbulent flow. Emmons² introduced the idea of turbulent spots that originate in more or less random fashion

and increasingly overlap as they enlarge during their transit downstream, finally covering the entire flowfield and resulting in fully turbulent motion. The passage of these spots over points on the surface results in alternations of laminar and turbulent flow. These alternations can be quantitatively described by an intermittency factor γ which represents the fraction of time any point spends in turbulent flow. Dhawan and Narashima³ showed that the intermittency factor can be used to predict the velocity profile and skin-friction variations within the transition region at subsonic speeds and that the origin of the turbulent boundary layer is approximately coincident with the onset of intermittency.

At supersonic speeds an analysis of a large body of heat-transfer data by Bertram and Neal⁴ has shown that the choice of the virtual origin at the point of peak shear or peak heating gave the most consistent results. The problem of choosing a consistent virtual origin is, however, far from resolved as evidenced in the discussion on boundary-layer transition at the AGARD meeting in May 1968.⁵ Thus it is felt that the more accurate location of onset, peak fluctuation level, and end of transition provided by heated thin film gages should help to resolve the difficulty of choosing consistent transition and virtual origin positions.

II. Subsonic Boundary-Layer Transition

Because of the importance of correctly determining the onset and extent of transition and the location of the virtual origin of the resulting turbulent boundary layer from wall

Presented as Paper 69-9 at the AIAA 7th Aerospace Sciences Meeting, New York, January 20-22, 1969; submitted February 24, 1969; revision received August 20, 1969. The work described in this report forms part of a program supported by the Ministry of Technology. The author wishes to express his thanks to B. J. Bellhouse and D. L. Schultz for their help and encouragement.

* Research Student, Department of Engineering Science; now Research Associate, NASA Ames Research Center, Moffett Field, Calif.